Article
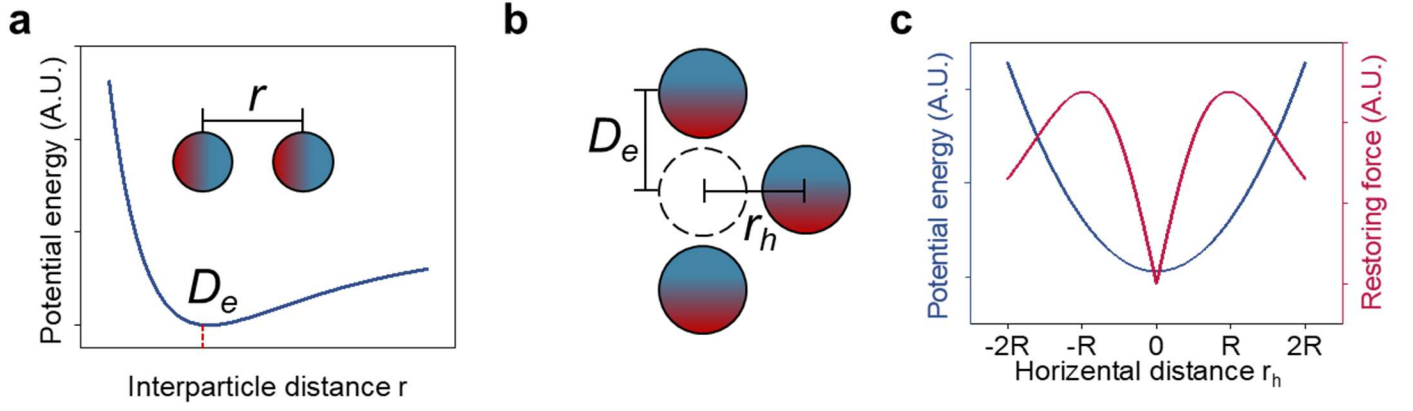
Permanent fluidic magnets for liquid bioelectronics

In the format provided by the
authors and unedited

Table of Contents

Supplementary Fig. 1. Potential energy profile and corresponding restoring force of nanomagnets in magnetic chain configurations. a, Potential energy profile of two nanomagnets with different interparticle distances along the dipole alignment direction. D_e is the equilibrium distance. **b**, Schematic of a translational perturbation occurring to the nanomagnet chain in the vertical direction. **c**, Potential energy and restoring force profile of the nanomagnets. R is the radius of the nanomagnets.
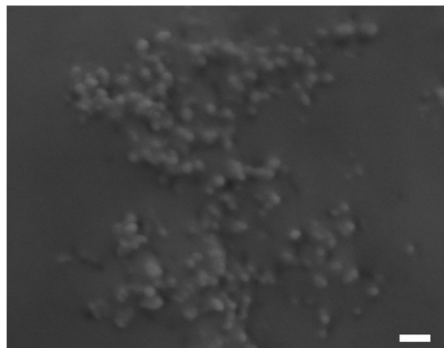
Supplementary Fig. 2. Scanning electron microscope (SEM) image of magnetic nanoparticles after sonication. Scale bar, 300 nm.
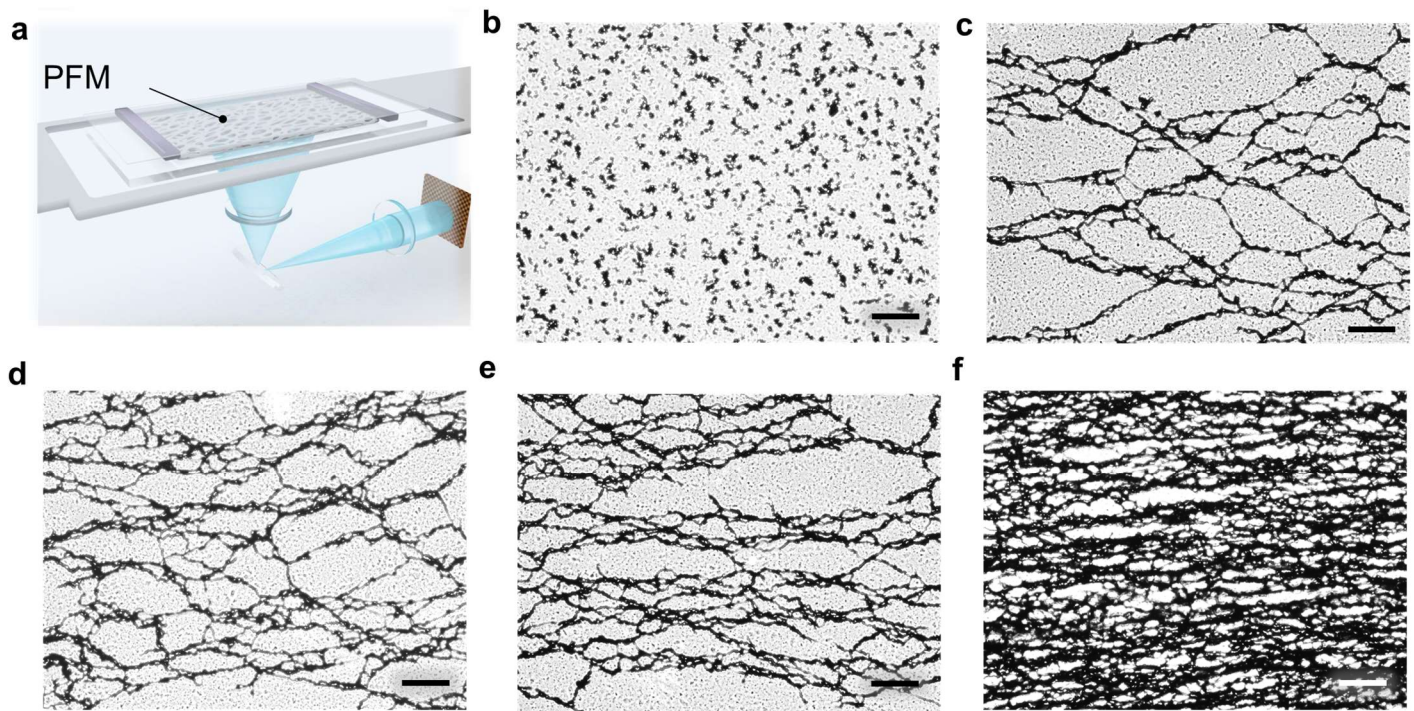
Supplementary Fig. 3. Microscope images of the 3D ORM network. a, The Schematic of the custom-made inverted optical microscopy. **b-f**, Microscope images of the cross-section of the 3D ORM network structure with the magnetization of (**b**) 3.7×10^3 Oe (**c**) 9.0×10^3 Oe (**d**) 9.1×10^3 Oe (**e**) 1.0×10^4 Oe (**f**) 2.5×10^4 Oe. Scale bars, 100 μm.
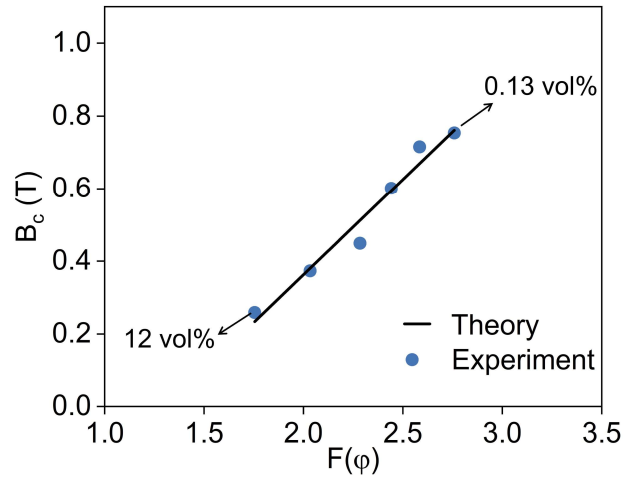
Supplementary Fig. 4. Linear relationship between the critical formation magnetic field and the function of concentration ($\sqrt{-ln\varphi - (1-\varphi)\ln(1-\varphi)/\varphi}$). It describes a decreasing trend in the critical magnetic field B_c with increasing volume concentration.
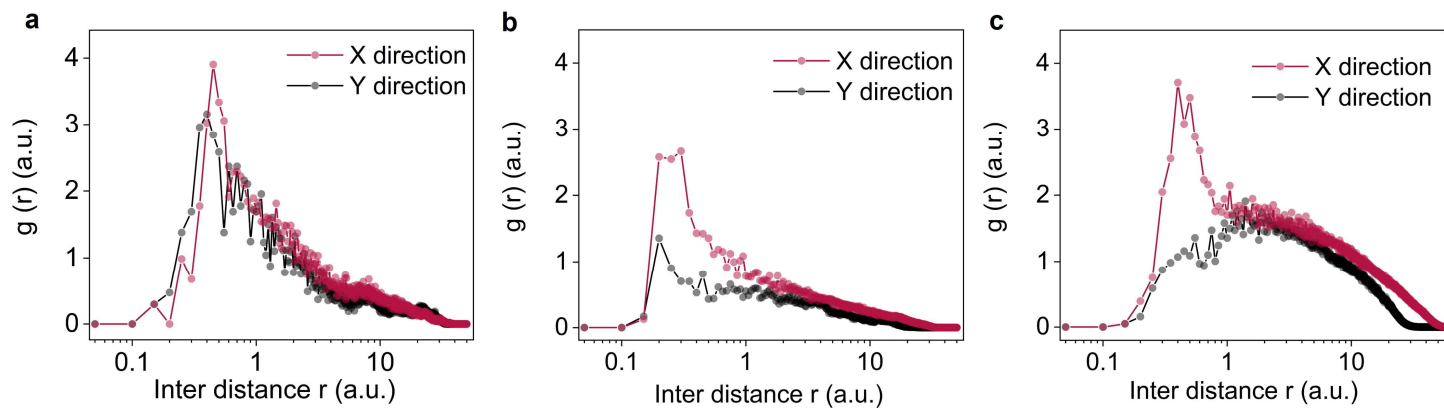
Supplementary Fig. 5. Calculation of directional pair correlation function (D-PCF) giving value *g*(r) in directions of X and Y axes after magnetization of **a**, 3.7×10^3 Oe, **b**, 8.2×10^3 Oe, and **c**, 1.0×10^4 Oe.
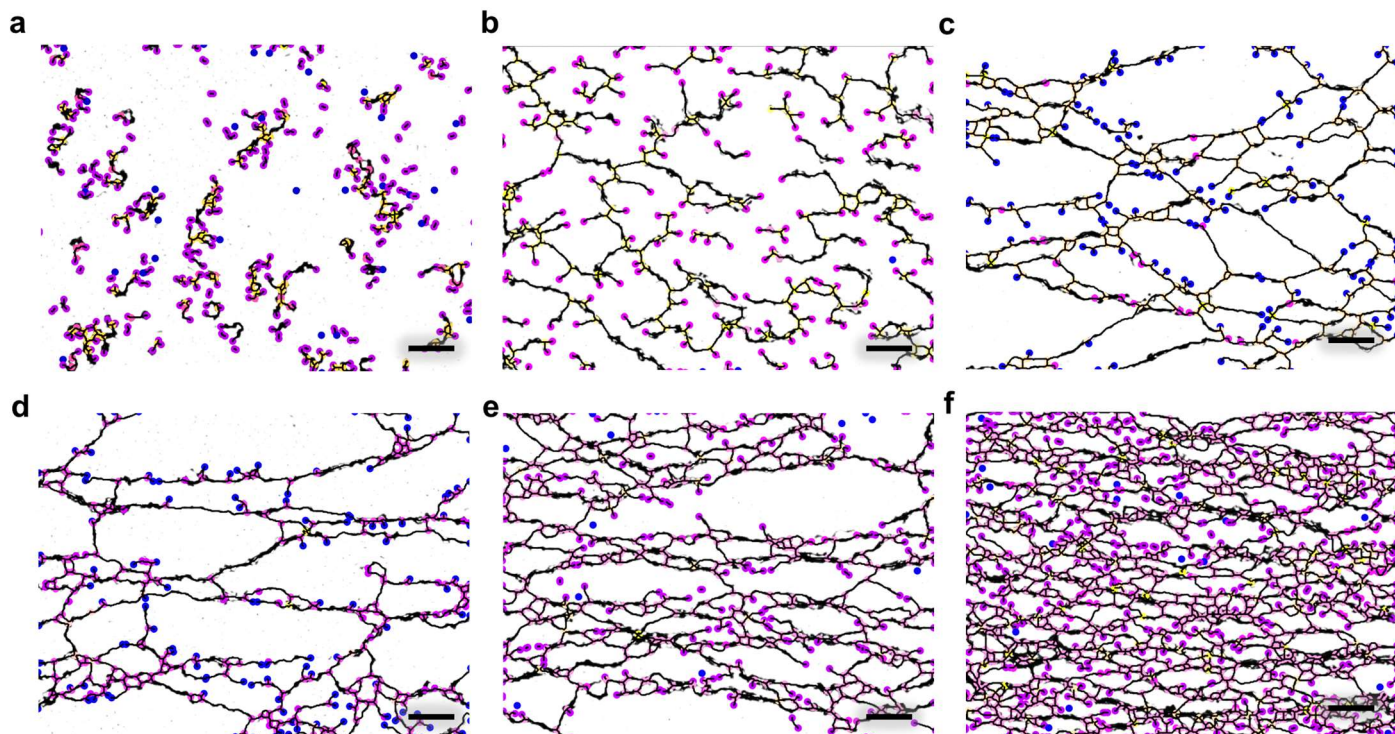
Supplementary Fig. 6. Connectivity of the 3D ORM network structure investigated by graph theory after magnetization of **a**, 3.7×10^3 Oe, **b**, 6.7×10^3 Oe, **c**, 9.0×10^3 Oe, **d**, 9.8×10^3 Oe, **e**, 1.0×10^4 Oe, and **f**, 1.1×10^4 Oe. Scale bars, 100 μm.
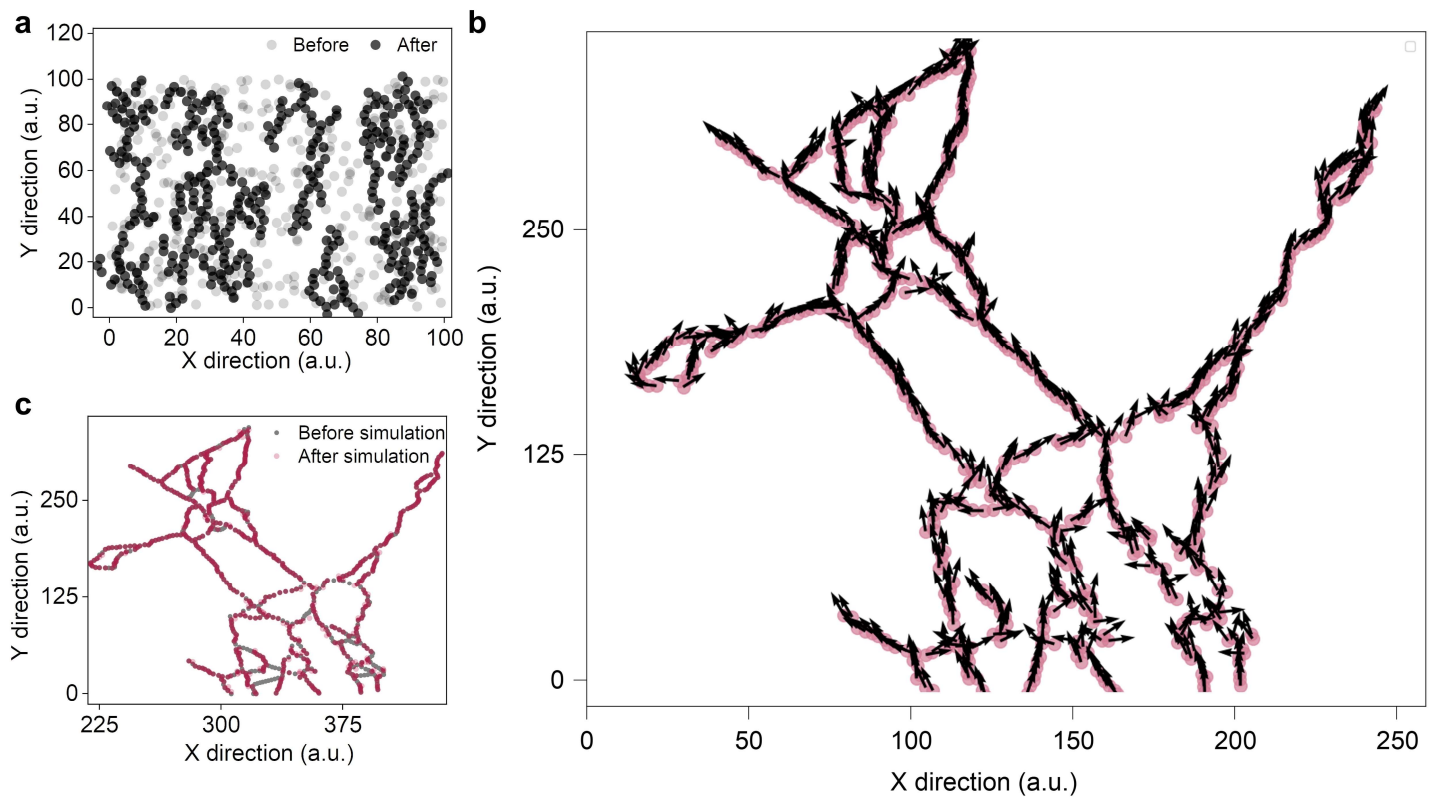
Supplementary Fig. 7. Monte-Carlo simulation of the 3D ORM network structure of the PFM. a, 3D ORM network can be formed with Monte-Carlo simulation indicating the network structure is thermodynamically stable. **b**, Monte-Carlo simulation network based on the optic image obtained in experiments. **c**, The PFM system under 100 V impulse magnetization before and after the Monte-Carlo simulation. The main shape of the ORM network structure can be well preserved during the simulated perturbation confirming the system stability.
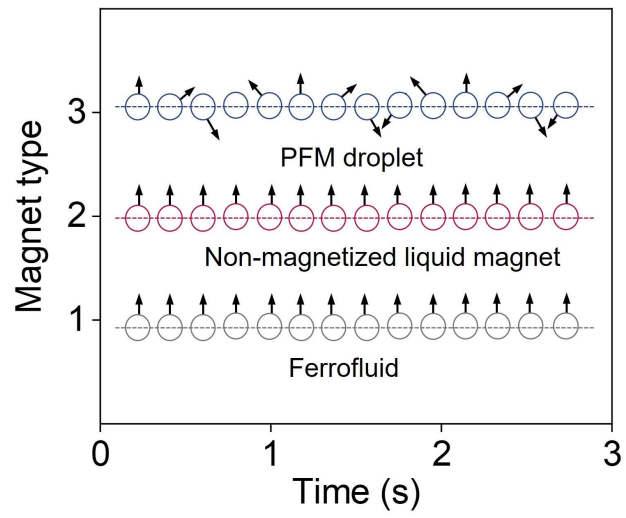
Supplementary Fig. 8. Motion status of the PFM droplet, non-magnetized liquid magnet, and ferrofluid buoyant in the water under a rotating magnetic field.
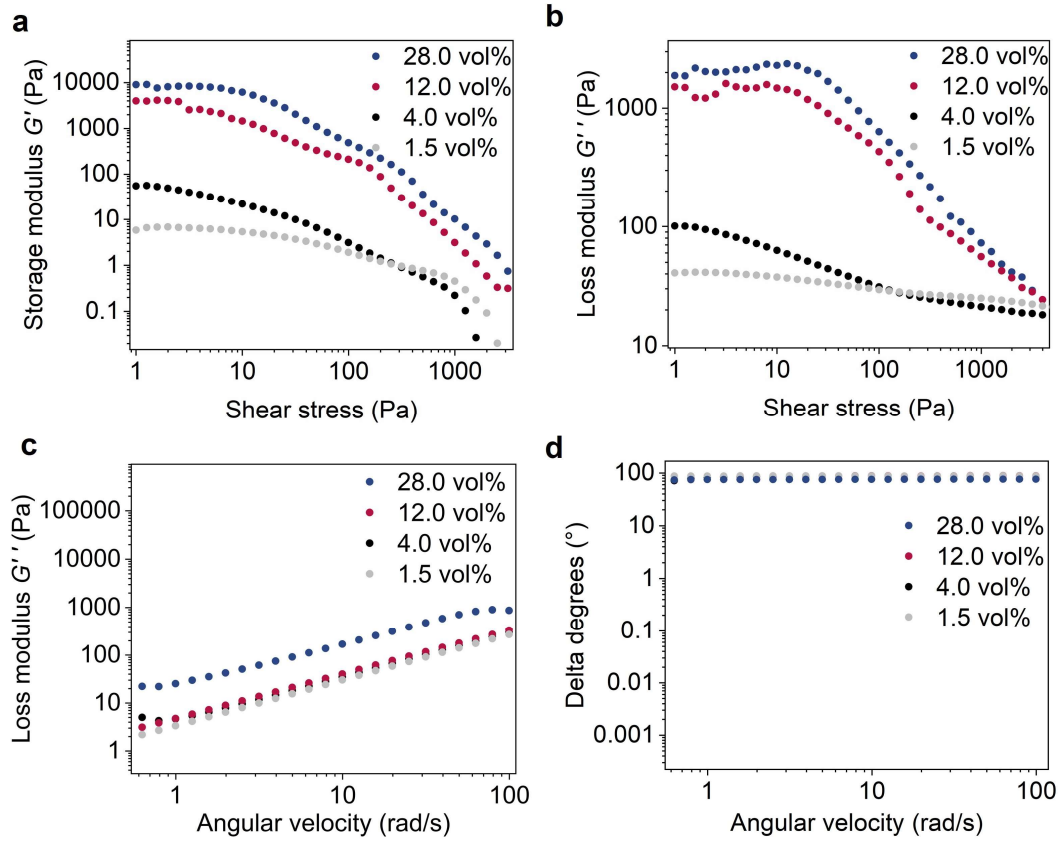
Supplementary Fig. 9. Rheological property of the PFM. The phase shift δ for all the samples at 2.5×10^4 Oe falls within the range of 45° to 90°, indicating a viscous fluidic behavior. a, Storage modulus as a function of shear stress after magnetization at 3.5×10^4 Oe. **b**, Loss modulus as a function of shear stress at 3.5×10^4 Oe. **c**, Loss modulus of the PFM as a function of shear rate after magnetization at 2.5×10^4 Oe. **d**, Delta degree of the PFM as a function of shear rate after magnetization at 2.5×10^4 Oe.
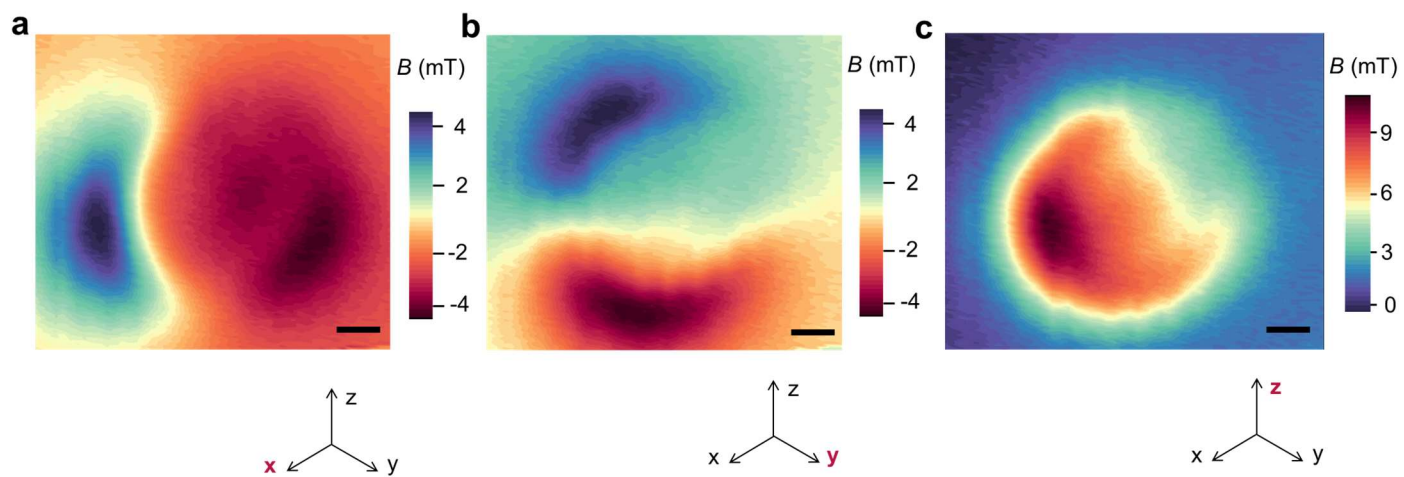
Supplementary Fig. 10. Magnetic mappings of the PFM. The magnetic mappings show its magnetic flux density in the **a**, x-axis, **b**, y-axis, and **c**, z-axis. Scale bars, 1 mm.
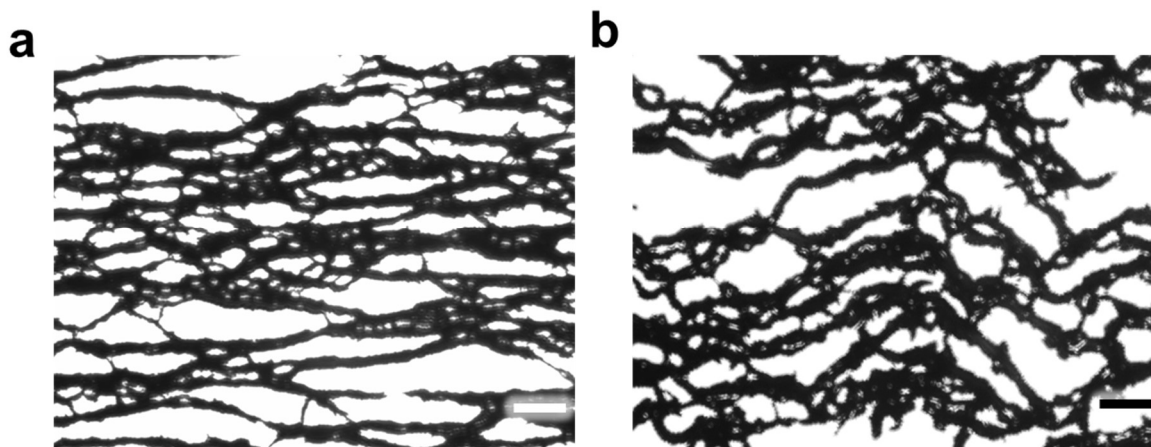
Supplementary Fig. 11. Images showing the rearrangement of the chain structure inside the PFM through the extrusion process. a, Before extrusion. **b**, After extrusion. Scale bars, 25 µm.
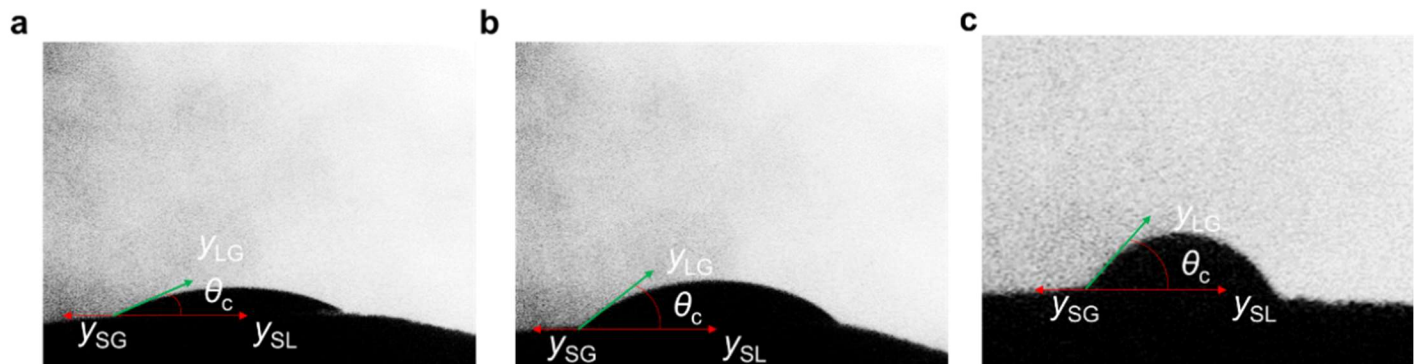
Supplementary Fig. 12. Investigation of static contact angle of the PFM on the pericardium surface of a rat model. **a**, The static contact angle of 1.5 vol% PFM, **b**, 4.0 vol% PFM, **c**, 12.0 vol% PFM.
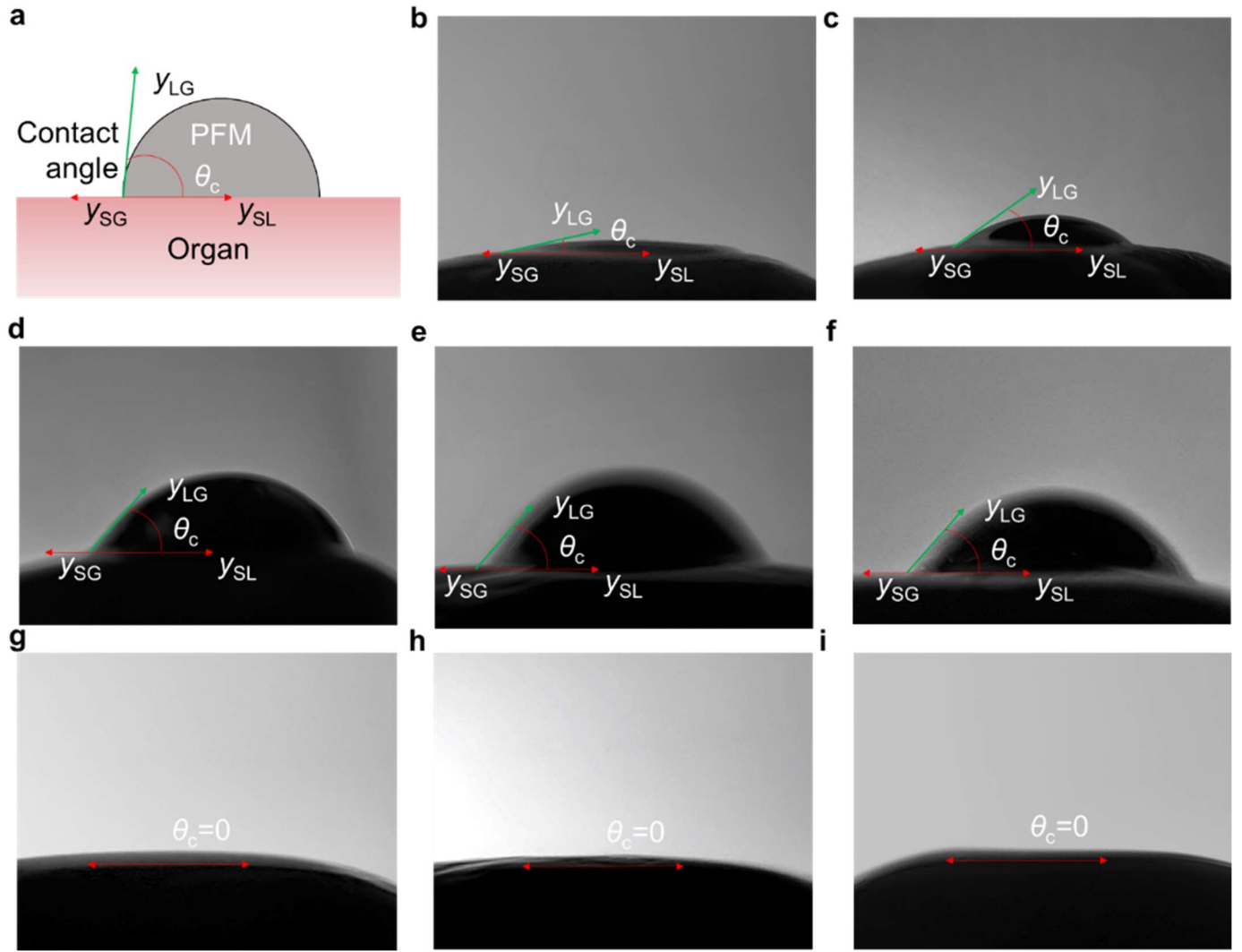
Supplementary Fig. 13. Investigation of static contact angle of various PFMs on different organ surfaces with live rats. **a**, Schematic diagram of the PFM on the organ surface. **b-d**, The static contact angle of PFM with carrier fluids' viscosity of (**b**) 1.0 Pa·s, (**c**) 9.12 Pa·s, and (**d**) 18.65 Pa·s on the heart surface of a live rat. **e-f**, The static contact angle of the PFM with carrier fluids' viscosity of 18.65 Pa·s on the (**e**) lung surface (**f**) and kidney surface of a live rat. **g-i**, The static contact angle of water on the (**g**) heart, (**h**) lung, and (**i**) kidney surfaces of live rats. It is found that the contact angle of the PFM droplet is nearly identical on different organ surfaces, likely due to the presence of similar serous membranes on the outer surface of these organs.
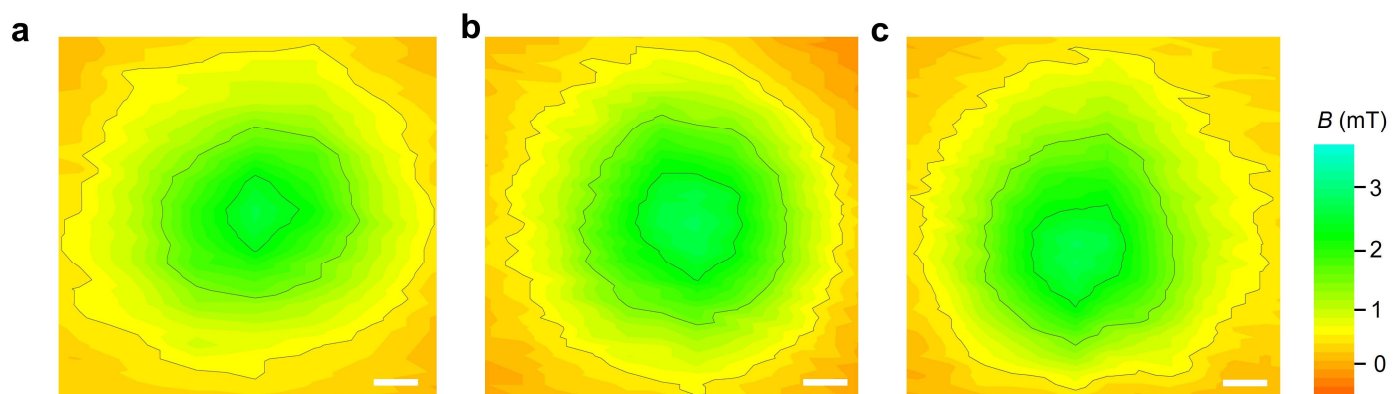
Supplementary Fig. 14. Magnetic profiles when identical PFMs were injected onto a, heart, **b**, lung, and **c**, kidney. Scale bars, 0.6 mm.
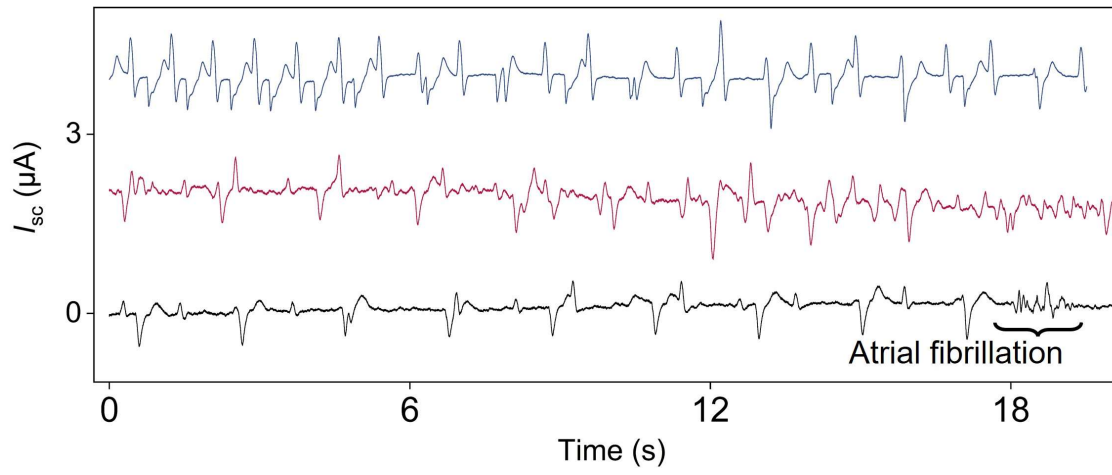
Supplementary Fig. 15. Generated cardiac signals show ventricular arrhythmia, atrial fibrillation, and irregular heartbeats.

a

b
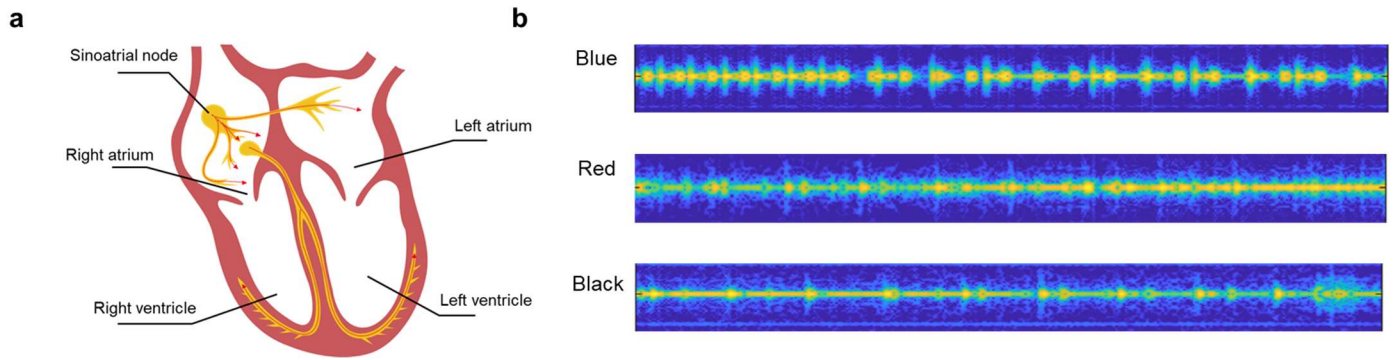
Supplementary Fig. 16. Illustration diagram of heart and analysis of the generated signals. a, Structure of the heart. **b**, The image of the short-time Fourier transform spectrograms generated from the measured electrical signals.
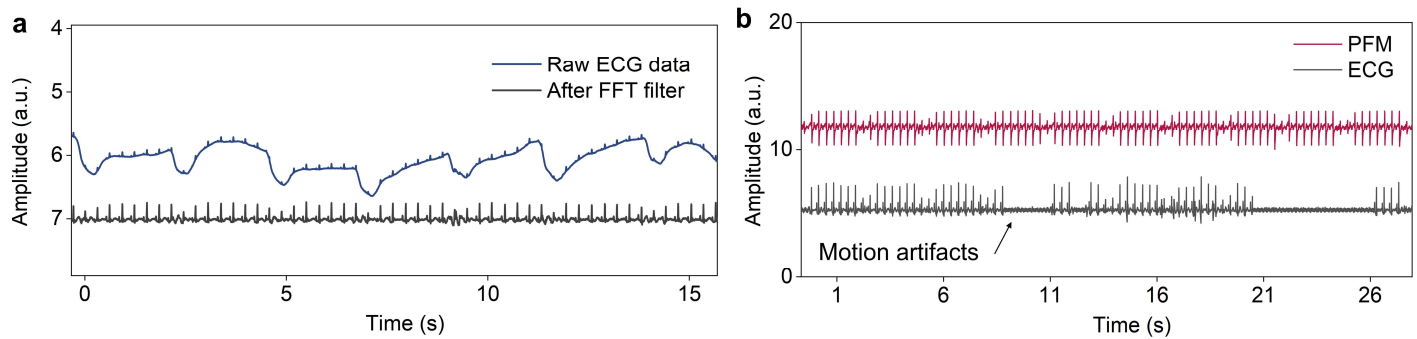
Supplementary Fig. 17. Stability assessment of liquid bioelectronics against motion artifacts and mechanical disturbance. a, The cardiac signal generated from the electrocardiogram. **b**, The cardiac signal generated from the electrocardiogram, and PFM-based liquid bioelectronics under motion artifacts and mechanical disturbance.

Supplementary Fig. 18. Biomechanical activities of the lung and liver were accurately measured by the generated electrical signals, and Fourier transform spectrograms were used to quantify the frequency information. a, Schematic illustration of the *in vivo* testing in rat's lung. **b**, Picture of the lung taken from the endoscope. Scale bar, 2 mm. **c**, The generated electrical signal from the regular movement of the lung. Inset is the image of the short-time Fourier transform spectrograms. **d**, Schematic illustration of the *in vivo* testing in rat's liver. **e**, Picture of the liver taken from the endoscope. Scale bar, 2 mm. **f**, Generated electrical signals from the movement of the liver. Inset is the image of the short-time Fourier transform spectrograms.

Supplementary Fig. 19. Capability of liquid bioelectronics for long-time *in vivo* testing.
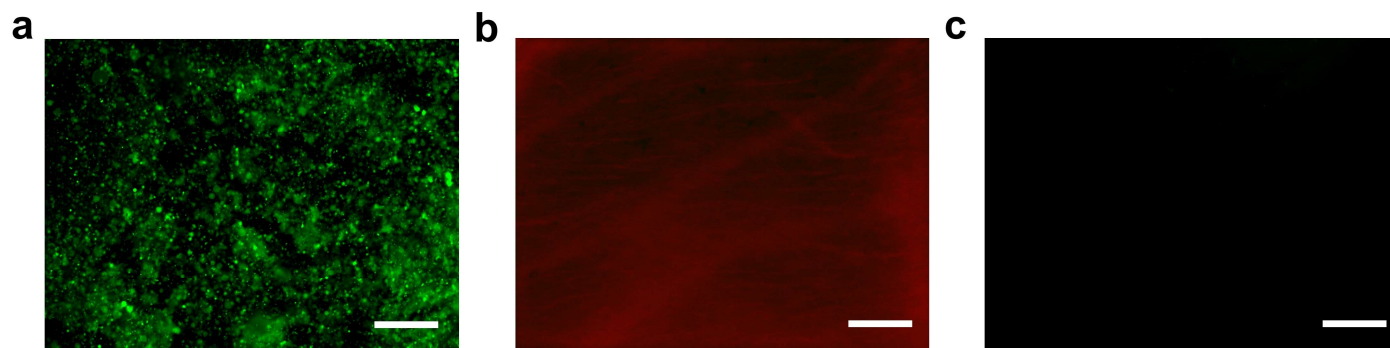
Supplementary Fig. 20. Fluorescent agent (Alexa Fluor™ 488, Invitrogen) was used to label the magnetic nanoparticles, which can be visualized using a fluorescence microscope. The magnetic nanoparticles were fully visualized after injecting the PFM onto the biological tissue surfaces. The fluorescent marks were barely visible after retrieval, demonstrating that the PFM can be fully removed from the biological tissue. **a**, Fluorescence microscope image of the biological tissue surfaces after injecting. **b**, Bright field microscope image of the biological tissue surfaces after retrieval. **c**, Fluorescence microscope image of the biological tissue surfaces after retrieval. Scale bars, 200 μm.
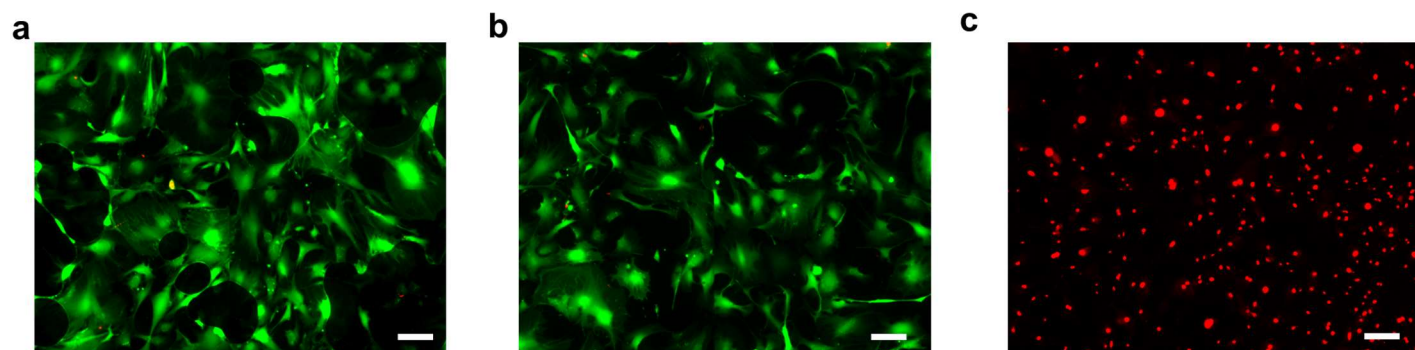
Supplementary Fig. 21. Live/Dead assay of human fibroblasts cultured for 24 hours. a, Positive control sample with cells being seeded in a cell culture dish. **b**, Cells cultured on the surface of the PFM. **c**, Negative control sample with cells being treated with 20% DMSO. Scale bars, 200 μm.
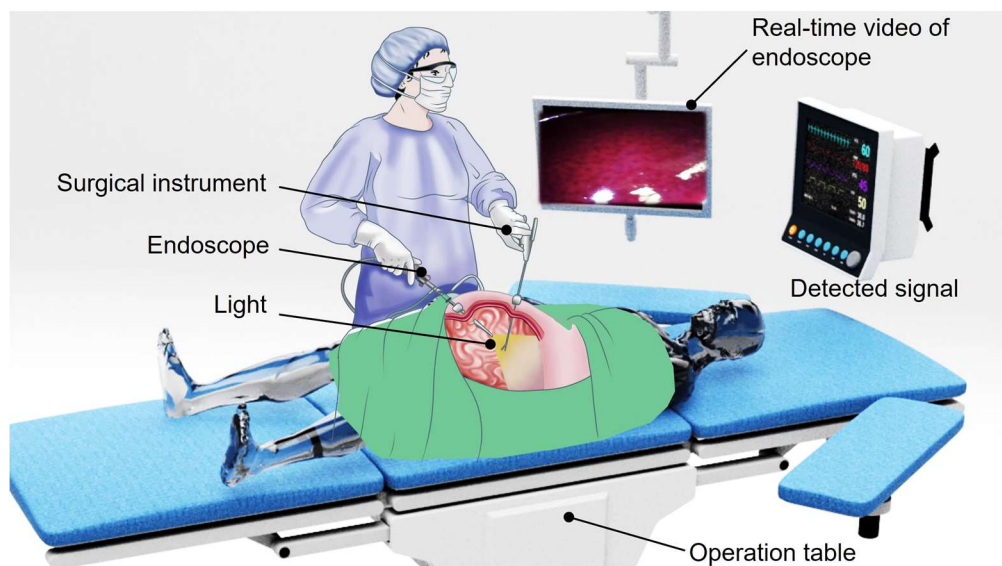
Supplementary Fig. 22. Demonstration of PFM-based liquid bioelectronics as a general method for physiological information extraction during minimally invasive surgery.

Supplementary Note 1. Potential energy analysis of nanomagnets

To explain the potential energy mapping of three nanomagnets arranged in different configurations, we assumed that the three nanomagnets possessed the same magnetization and fixed two nanomagnets at the position of (D_e, 0) and (-D_e, 0), respectively, where D_e is the equilibrium distance of two nanomagnets calculated using a hard sphere model and the truncated Lennard Jones potential. D_e is dependent on the cutoff radius of the truncated Lennard Jones potential and can be calculated to be $2^{7/6} R$, where R is the radius of the nanomagnets. Then, we changed the position of the third nanomagnet and calculated the total potential energy of the system to obtain the mapping potential energy profile. As illustrated in Supplementary Fig. 23a, when the third nanomagnet is set at (0 , 0) and the three nanomagnets form a straight line, the system's potential energy is the lowest, corresponding to the red point (0 , 0) in Supplementary Fig. 23b. Similarly, when the third nanomagnet is placed at (D_e, D_e) as illustrated in Supplementary Fig. 23c, the system's potential energy corresponds to the red point (D_e, D_e) in Supplementary Fig. 23d. Thus, in the potential energy profile, each point corresponds to the potential energy of a unique configuration of three nanomagnets positioned at (-D_e, 0), (D_e, 0), and (x, y), respectively, where x and y represent the coordinates on the graph.
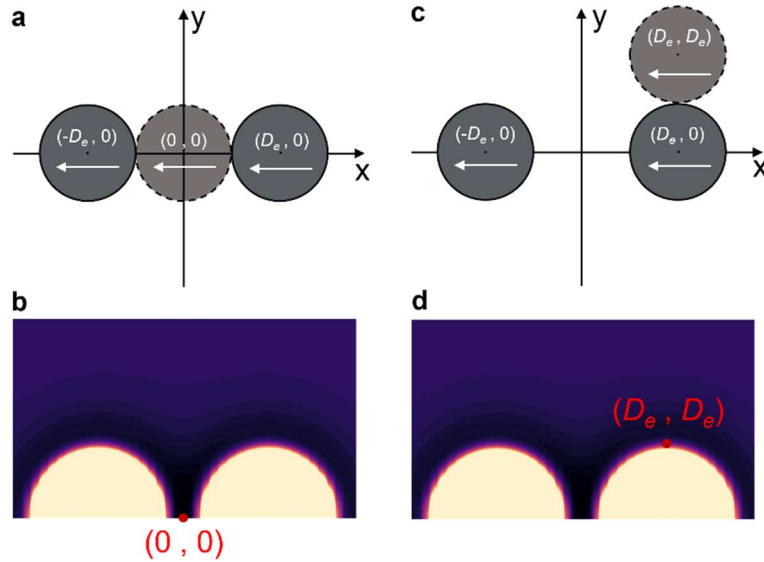
Supplementary Fig. 23. Potential energy mapping of three nanomagnets aligning in various configurations. **a**, Configuration that the third nanomagnet is placed at (0 , 0) and the three nanomagnets align in a straight line. **b**, Mapping of the system potential energy with (0 , 0) marked by the red point, which corresponds to the configuration in (**a**). **c**, Configuration that the third nanomagnet is placed at (D_e, D_e). Two nanomagnets are aligned in a vertical line with parallel magnetization and the other nanomagnet locates at (-D_e, 0). **d**, Mapping of the system potential energy with (D_e, D_e) marked by the red point, which corresponds to the configuration in (**c**).

Supplementary Note 2. The influence of carrier fluid viscosity on the stability of the 3D ORM network

To investigate the influence of carrier fluid viscosity on the stability of the 3D ORM network structure in the PFM systems, we dispersed the magnetic nanoparticles inside carrier fluids with different values of viscosity ranging from 19.68 Pa·s to 0.01 Pa·s (Supplementary Fig. 24a). Their corresponding cross-section microscope images are shown from Supplementary Fig. 24b to Fig. 24f, respectively. As shown in Supplementary Fig. 24b-d, the 3D ORM network structure remained stable, and the nanoparticles remained suspended in higher viscosity fluids (> 2 Pa·s). This is due to that the high-viscosity fluids could limit the drift of the nanomagnets during the magnetic-field-guided self-assembly process, promoting the formation of a stable 3D ORM network. In contrast, the 3D ORM network formation in lower viscosity fluids (< 1Pa·s) is less efficient, resulting in nanoparticle aggregation, as depicted in Supplementary Fig. 24f.
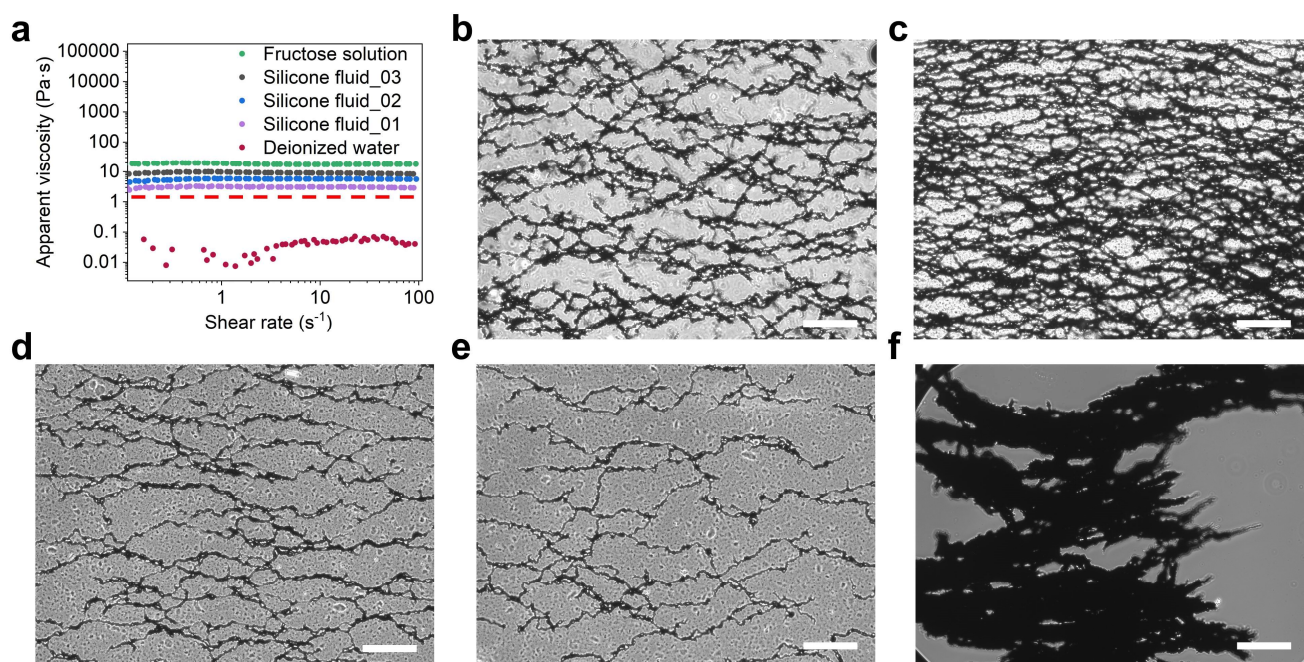
Supplementary Fig. 24. Microscope images of the 3D ORM network structure of the PFM with different carrier fluids. a, Apparent viscosity plotted against the applied shear rate for different carrier fluids. **b-f,** The cross-section microscope image of the 3D ORM network structure with (**b**) fructose solution as the carrier fluid, (**c**) silicone fluid_03 as the carrier fluid, (**d**) silicone fluid_02 as the carrier fluid, (**e**) silicone fluid_01 as the carrier fluid, (**f**) deionized water as the carrier fluid. Scale bars, 100 μm.

These findings strongly indicate that the viscosity of the carrier fluid shows an impact on the stability of the PFM system. On one hand, carrier fluids with higher viscosity help limit the diffusion length of the nanomagnets during the magnetic-field-guided self-assembly, which promotes the formation of the 3D ORM network structure. On the other hand, the higher viscosity increases the kinetic barrier of the nanomagnets within the ORM network structure, hindering their motion in response to hydrodynamic interactions and thereby improving the stability of the PFM system.

Supplementary Note 3. Monte-Carlo simulation of the formation process of the 3D ORM network structure

We performed the Monte-Carlo simulation to help understand the formation process of the ORM network structure. Instead of using single nanomagnets, the Monte-Carlo simulation here applied nanomagnets clusters as the basic moving element. All the clusters are considered as dipolar hard spheres with pair interaction potential composed of dipole-dipole interaction and truncated Lennard-Jones potential[2,3], then the total energy of the system U can be written as below,

$$U = 4\varepsilon_0 \sum_{i,j,\ i \neq j} \left\{ \frac{2R}{r_{ij}^{12}} - \frac{2R}{r_{ij}^{6}} - \frac{2R}{r_c^{12}} + \frac{2R}{r_c^{6}} \right\} - \frac{2}{3}\pi R^3 \mu_0 \sum_i \left\{ \frac{1}{\chi}M^2 + R^3 \sum_{j,\ j \neq i} \left[\frac{(\vec{M} \cdot \vec{r}_{ij})(\vec{M} \cdot \vec{r}_{ij})}{r_{ij}^{5}} - \frac{M^2}{3r_{ij}^{3}} \right] \right\}$$

where ε_0 is the vacuum permittivity, R is the radius of the cluster, $\vec{r}_{ij}$ is the displacement vector between the ith and j^{th} clusters, r_c is the cutoff radius and equals $2^{7/6}R$, μ_0 is the vacuum permeability, χ is the susceptibility of the nanomagnet, and M is the magnetization of the nanomagnet. The simulation was performed in a system of 400 nanomagnet clusters with a radius of 1.5 μm and magnetization of 6×10^5 A/m. Starting from a randomly distributed state, during each simulation step, a random cluster will be picked up and assigned with one small rotation angle of 2 degrees and translation movement of 1.5 μm. Each Monte-Carlo step will be accepted if it yields lower total energy, or falls into the probability of exp($-\Delta E/k_{BT}$). To accelerate the simuation process and avoid getting trapped in a local minimum, clusters with an interdistance less than 1.2 times the cluster diameter are treated as an assembly during the simulation. Totally 30,000 steps were performed for the system to reach equilibrium. Based on the Monte-Carlo simulation results, it is clear that an ORM network structure can be formed in the simulation similar to the experimental results from the observation of the optical image. The simulation results confirm that the ORM network structure is the most energetically favorable configuration of the PFM system. We further examined the stability of the PFM system by perturbing the formed ORM network. For the simulation initialization, the position of each nanomagnet cluster was determined by the digital mapping of optical images. The initial magnetization of each cluster was assigned to be 6×10^5 A/m with the orientation determined by its nearest two neighbor clusters inside the network structure. A total of 604 clusters with a radius of 1.5 μm were considered in the system.

Supplementary Note 4. Different motions of PFM under external magnetic fields

A distinctive characteristic of the PFM is its reconfigurability while maintaining a degree of permanent magnetism, which sets it apart from other paramagnetic magnetic fluids, such as ferrofluids. We conducted experiments to investigate the different motions of various magnetic fluids under external magnetic fields at both microscopic and macroscopic scales. We built a magnetic drive system consisting of one or two identical magnets to generate magnetic forces in alternating directions to drive PFMs.
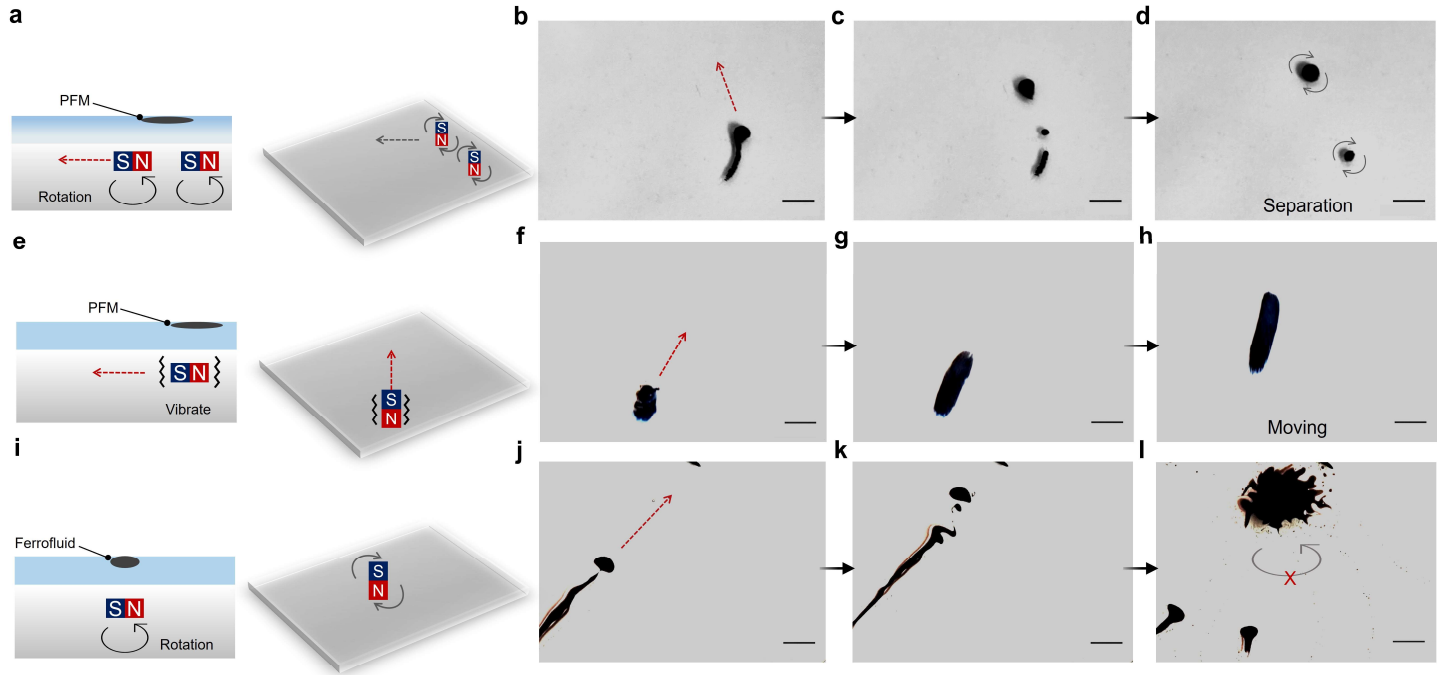
Supplementary Fig. 25. Different motions of PFM and ferrofluid under external magnetic fields in a macroscopic view. a, Schematic diagram of the magnet field's dispersion. **b-d**, Macroscope images of the PFM separation under an external magnetic field. Scale bars, 5 mm. **e**, Schematic diagram of the magnet field's dispersion. **f-h**, Macroscope images of the PFM slenderizing forward under an external magnetic field. Scale bars, 5 mm. **i**, Schematic diagram of the magnet field's dispersion. **j-l**, Macroscope images of the ferrofluid under external magnetic field. Ferrofluids did not rotate along with the external magnetic field. Scale bars, 10 mm.

In the macroscopic view, the PFM exhibited varied motions and rapid transformations when subjected to external magnetic fields. The separation of two external rotating magnets caused the produced PFM to separate (Supplementary Fig. 25a-d); while a vibrating magnet caused the PFM to move (Supplementary Fig. 25e-h). Those experiment results prove that PFM can realize the untapped combination of reconfigurability and ferromagnetism in a single material system. We also compared its performance to other non-permanent fluidic magnets, such as ferrofluids. While the ferrofluids showed reconfigurability as they approached the rotating magnet (Supplementary Fig. 25i-l), they did not exhibit ferromagnetism as they did not rotate along with the external magnetic field (Supplementary Fig. 25l).
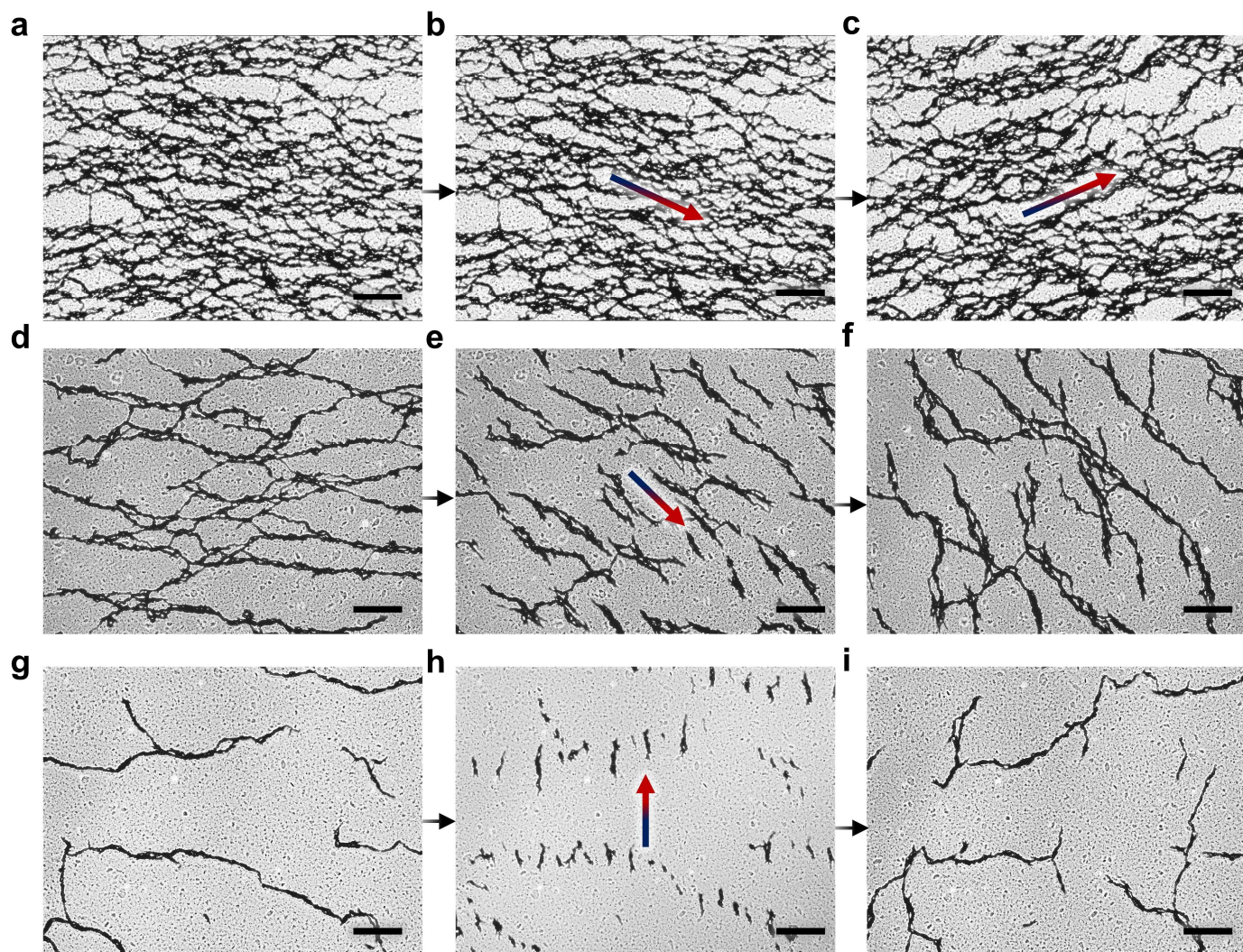
Supplementary Fig. 26. Different motions of ORM networks under external magnetic fields in the microscopic view. a-i, ORM networks in (**a-c**) 12.0 vol%, (**d-f**) 4.0 vol%, and (**g-i**) 1.0 vol% PFM dynamically disassemble, and reassemble under the external magnetic field. Scale bars, 100 μm.

In a microscopic view, the 3D ORM network can dynamically disassemble under the external magnetic field and reassemble independently. The 3D ORM network of PFM with a concentration of 12.0 vol% was reconstructed along with an external magnetic field (Supplementary Fig. 26a-b), and it restored its ORM network after self-assembly (Supplementary Fig. 26c). Similarly, samples with lower concentrations of 4.0 vol% and 1.0 vol% also restored their 3D network after external magnetic fields disrupted their structure (Supplementary Fig. 26d-f and Fig. 26g-i).

Supplementary Note 5. Finite element simulation to study the effect of magnetic repulsion between chains within the ORM network during the gravity-induced consolidation

The stability of the PFM can be understood by the magnetic force $F = \nabla(\vec{m} \cdot \vec{B})$ and the potential energy $U = U_{lj} - \vec{m} \cdot \vec{B}$ of the nanomagnets, where U_{lj} is the truncated Lennard-Jones potential[4], $\vec{m}$ is the magnetic moment of the nanomagnet, and $\vec{B}$ is the magnetic flux density exerted by other nanomagnets using a standard magnetic dipole model[5]. For nanomagnets with 100 nm diameter, we calculated the potential energy profile and magnetic force of a single nanomagnet in the network configuration using the nearest neighbor approximation. Our results show that the adoption of hard nanomagnets with strong coercivity (*e.g.*, 6×10^5 A/m) will lead to a magnetic dipole force 10^7 times of the gravity force once the network structure is formed and nanomagnets aligned in a head-to-tail configuration. As a result, the settling effect of single nanomagnets is efficiently mitigated. Only the gravity of the whole network needs to be considered. The potential energy mapping profiles of nanomagnets and the restoring force in the vertical direction are shown in Fig. 1g and Supplementary Fig. 1c, respectively. It can be seen that the nanomagnets inside the network are in their equilibrium states (*i.e.*, in a potential well) so that any translational motions of the nanomagnets will be mitigated by the restoring forces. These results are in agreement with the simulation results in Supplementary Note 3.

Subsequently, we examined how the 3D ORM network can withstand gravitational collapse by means of deforming its overall structure. Specifically, the gravitational stress intends to compress or consolidate the 3D ORM network structure of the PFM. However, the network structure can distribute the stress throughout and resist such deformation in two approaches. The first is the stretch and compression of the chains in the network. In this way, because the magnetic clusters are in their equilibrium states, although the gravitational stress can lead to a deviation of their state from the equilibrium, they possess a restoring force that enables them to store deformation energy elastically and resist gravitational stress. The second is the rotation of the chains inside the network structure. During this process, the magnetic repulsion between the chain plays a significant role. We calculated the magnetic energy density of a two-dimensional periodic network structure with different angles relative to the vertical direction in Supplementary Fig. 27a. In the simulation, we assume that the magnetization direction of each magnetic cluster is aligned with the chain direction. Consequently, when the network configuration changes from a high angle to a low angle, it can be considered as the rotation of the chain due to consolidation caused by gravity within the network structure. Through the simulation, we observed an increase in the magnetic energy density of the system (Supplementary Fig. 27b), when rotating the network structure. This increase of magnetic energy can be ascribed to the work done by magnetic repulsion forces during the rotation process. Thus, it indicates that the magnetic repulsion between the chains plays a role in supporting the buoyant weight of the network structure and defying gravity. Overall, we consider the ability of the PFM to resist gravitational deformation as a result of the elasticity and rigidity of the arising percolated network structure. This rigidity of

the network structure is featured by the decrease in the degree of freedom (DOF) of the nanomagnets inside the network.
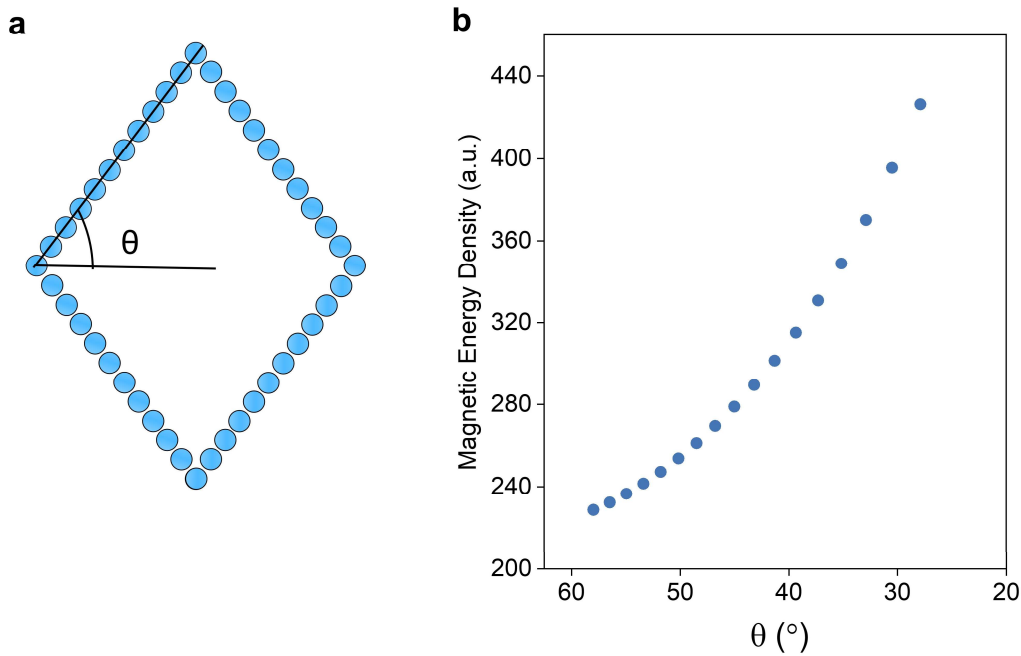
Supplementary Fig. 27. Finite element simulation to study the effect of magnetic repulsion between chains within the ORM network during the gravity-induced consolidation. a. Repeating unit of a 2-dimensional periodic structure to study how chain rotation influences the magnetic energy of the whole structure under gravity-induced consolidation. **b**. Calculated magnetic energy density of the 2D periodic network structures with different degrees of orientation with respect to the vertical direction.

Overall, the above analysis points out that the stability of the PFM relies on the network's ability to support its buoyant weight instead of the stability of the single nanomagnet inside the network structure, which has been verified in weak attractive colloids[6-8]. Stretching, compression, and rotation of the network chains all provide repulsive magnetic forces to resist the gravitational collapse of the whole network structure.

It is worth further emphasizing that the magnetic repulsion between the chains could play a significant role in maintaining the network structure of the PFM and distinguishing it from other network-structured colloids formed by van der Waals attraction and depletion attraction. The origin of the magnetic repulsion between the chains arises from the directional particle-particle interaction which is unique in the dipolar system. It may be the key to the superior stability of the PFM. In the long-term experiment (i.e., in the time scale of around one year), we did not observe coarsening nor sudden collapse of our ORM network structure, which often occurs in the colloidal networks based on isotropic van der Waals attraction. Such coarsening and sudden collapse are ascribed to the diffusive migration of particles in a liquid-like surface, which is energetically favorable, although kinetically unfavorable[9]. In fact, colloidal networks based on van der Waals attraction are nonequilibrium assemblies formed by diffusion-limited dynamic arrest. Their thermodynamic ground state corresponds to the macroscopic separation of a particle-rich and a particle-poor phase. However, the assembly of the ORM network may be a

combination of thermodynamic and kinetic processes. It is possible that the ORM network structure is thermodynamically favorable because of the directional dipolar and multipolar interactions, which has been partially verified by our Monte-Carlo simulation (Supplementary Note S4). Surface migration of nanomagnets on the ORM network of our PFM may be energetically unfavored. This may hold the key to achieving long-term stability in the ORM network and ensuring the consistent magnetic properties of our PFM.

Supplementary Note 6. Evaluating the PFM stability with the poroelastic theory

Macroscopically, the ability of the PFM to maintain stability and defy gravity can be characterized by the storage modulus of the PFM. We utilize a simple framework[10] to quantify the stability of our network-structured PFM. Although this framework was originally developed to describe the collapse of network structures induced by van der Waals attraction in the silica colloid, it relies on the concepts of poroelasticity in the formed network structure and Darcy's law, both of which do not directly consider the detailed particle-particle interactions. Thus, it can be generalized into our system. According to the framework, the consolidation of the network structure under gravity is associated with the deformation of the network $w(z, t)$ and the expulsion of interstitial fluid from the network due to pressure P. Thus, the constitutive equation for a poroelastic system can be written as,

$$\sigma = E\frac{\partial w}{\partial z} - (1 - \Phi)P \tag{1}$$

where Φ is the volume ratio of the network structure and E is the storage modulus. With only gravity as the stress origin, the stress gradient satisfies the following balance,

$$\frac{\partial \sigma}{\partial z} = -\Delta \rho g \Phi \tag{2}$$

where $\Delta \rho$ is the density difference between the fluids and the nanomagnets, and g is the gravitational acceleration. With appropriate initial and boundary conditions, the equation can be solved using the separation of variables and the height of the ORM network structure in the PFM $h(t)$ at time t can be expressed as,

$$h_0 - h(t) = \Delta h \left(1 - e^{\frac{-t}{\tau}}\right) \tag{3}$$

where h_0 is the initial height of the network structure, τ is the time scale for the collapse, and Δh is the total change of the network height, which can be expressed as below,

$$\Delta h = \frac{\Delta \rho g \Phi h_0^2}{2E} \tag{4}$$

We calculate the change of the network height using parameters of our system including $\Delta \rho$ of 6.6×10^3 kg m^{-3}, g of 9.8 m s^{-2}, Φ of 0.04, E of 55.09 Pa from the rheological measurement, and h_0 of 2 mm. We obtain that $\Delta h/h_0$ equals to 4.70% indicating that the network structure of our PFM will only deform 4.70% of its original height after its initial formation. Hence, our PFM will be able to resist gravity deformation and remain stable with the poroelasticity from the ORM network structure. It is worth noting that the stability of the PFM is closely linked to its initial height. As the height of the PFM increases, its gravitational stability decreases proportionally, which is reasonable since the larger gravitational stress acts on a network with constant elasticity.

Supplementary Note 7. Calculating the compressional yield stress of the PFM

This ability of the ORM network to convey stress throughout the network structure and support its buoyant weight can be characterized by the compressional modulus and compressional yield stress P_y[6-8]. A critical condition to ensure the stability of a static network-microstructured colloid is $P_y \geq \Delta\rho g H\varphi$, where $\Delta\rho g H\varphi$ is the static stress at the bottom of the colloid. $\Delta\rho$ is the density difference between the nanomagnets and the carrier fluid, g is the gravitational acceleration, H is the height of the colloid, and φ is the volume concentration of the nanomagnets. The $\Delta\rho g H\varphi$ of 1 cm height, 4 vol% PFM system is calculated to be 26 Pa. The value of P_y is evaluated using the shear yield stress σ_y, which can be extrapolated from the trend of the storage modulus in the rheological test. It has been pointed out that P_y is usually one order of magnitude larger than σ_y in a network structure with spherical particles[8]. From Supplementary Fig. 9, it can be intuitively inferred that σ_y is approximately 10 Pa. As a result, P_y is at the level of 100 Pa, much higher than the 26 Pa critical point. Thus, the analysis points out that the ORM network is stable, which is also in good agreement with the experimental results.

Supplementary Note 8. Calibrating electrical signals from the PFM based liquid bioelectronics

To obtain interpretable electrical signals from the injectable PFM liquid bioelectronics, a calibration process is developed as below,

1. Calibrate the shape and magnetization distribution of the injected PFM on various tissue surfaces *ex vivo*. The shape of the PFM will be determined by first controlling its injected volume and then measuring its contact angle on various tissue surfaces. The magnetic field profiles of the injected PFM droplet will be measured with a customized printed circuit board (PCB) mounted with a hall sensor array (MLX 90393, Melexis) with an improved resolution of 0.161 μT.

2. Calibrate the distance between the site of the injected PFM and the small incision where the endoscope is inserted. A specially designed injection syringe with a graduated scale together with an endoscope will be used to evaluate the distance between the injected PFM and the conformal coil. The center of the coil will be placed over the small incision to ensure a fixed orientation between the PFM and the coil.

3. Calibrate the 3D configuration of the conformal coil after it conforms to the mouse skin.

Supplementary Note 9. A theoretical model to obtain the localized movement of the internal tissue

From the viewpoint of Faraday's Laws of Electromagnetic Induction, the induced electromotive force (EMF) in multiple coils can be regarded as the summation of EMF obtained in each coil. The corresponding equation is demonstrated below,

$$\varepsilon_t = \sum_{i=1}^{n} \varepsilon_i = \sum_{i=1}^{n} -\frac{d\Phi_i}{dt} \tag{1}$$

where ε_t is the total EMF, n is the total number of the coil, ε_i is the EMF induced in each coil, and Φ_i is the magnetic flux through each coil. In our measurement setting, the short circuit current is used as the electrical signal, which yields,

$$I_{sc} = \frac{\varepsilon_t}{R} = \sum_{i=1}^{n} -\frac{d\Phi_i}{Rdt} \tag{2}$$

where I_{sc} is the total short circuit current in the coil and R is the total internal resistance of the coil. When the coil is rigid and each loop in the coil has the same diameters, the above equation then converges to the common Faraday's law of induction as below,

$$\varepsilon_t = -n\frac{d\Phi_b}{dt} \tag{3}$$

where Φ_b is the magnetic flux of a single loop. For our liquid metal coil, each loop will have a different diameter because of the in-plane design. In addition, during the coil attachment process, the liquid metal coils will be deformed to conform to the skin and thus each loop will evolve to a 3D configuration. To calculate the EMF of each loop with a different diameter and a 3D configuration in our liquid metal coil, it is necessary to use the vector product and the magnetic flux density in each loop, which can be expressed as,

$$I_i = -\frac{d\Phi_i}{Rdt} = -\frac{d\iint \vec{B} \cdot d\vec{A_i}}{Rdt} \tag{4}$$

where I_i is the current contribution from every single loop, $\vec{B}$ is the magnetic flux intensity, and $d\vec{A_i}$ is the area element of the single loop. By summing the contribution from all loops, the total short circuit current of our conformal liquid metal coil can be calculated.

After establishing the relationship between the short circuit current and the magnetic field of the arbitrary conformal coil, we develop the model of the time-varying magnetic field of the PFM system when attached to the internal tissues. First, it is reasonable to assume that the PFM is aligned with the center of the liquid metal coil and moves in the aligned direction due to the contraction-relaxation cycle of the internal tissue (e.g., heart) and the relatively small size of our PFM droplet (e.g., ~ 4 mm diameter).

Then, the magnetic field distribution of an arbitrary PFM droplet on the internal tissue can be solved using Poison's equation with Green's Function, through which the magnetic potential φ can be expressed as,

$$\varphi(\vec{r}) = \int \rho G(\vec{r}, \vec{r'}) \, d\vec{r'} \tag{5}$$

where ρ is the effective magnetic charge density equaling $-\nabla \cdot \vec{M}$, in which $\vec{M}$ is the magnetization distribution of the PFM, which can be obtained from the calibration process. G is the green's function with the following form,

$$G(\vec{r}, \vec{r'}) = \frac{1}{4\pi |\vec{r} - \vec{r'}|} \tag{6}$$

Then, the magnetic flux density distribution $\vec{B}$ of the PFM can be expressed,

$$\vec{B}(\vec{r}) = -\mu_0 \nabla \varphi(\vec{r}) \tag{7}$$

We consider the spatial distribution of $\vec{B}$ as a function of time t. For simplicity, we can set the aligned direction as the z direction. Thus, the localized movement of the mouse heart $f(t)$ that was measured by our PFM can cause a variation of the magnetic potential, which be expressed as,

$$\varphi(\vec{r}, t) = \varphi(\vec{r} - f(t)\vec{k}) \tag{8}$$

Combining equations 2, 4, 7, and 8, we can obtain,

$$I_{sc}(t) = \sum_{i=1}^{n} -\frac{d\Phi_i}{Rdt} = \sum_{i=1}^{n} \frac{\mu_0 d \iint \nabla \varphi(\vec{r} - f(t)\vec{k}) \cdot d\overrightarrow{A_i}}{Rdt} \tag{9}$$

Integrating equation 9 with respect to time,

$$\int I_{sc}(t)dt = \frac{\mu_0}{R} \sum_{i=1}^{n} \iint \nabla \varphi(\vec{r} - f(t)\vec{k}) \cdot d\overrightarrow{A_i} \tag{10}$$

In order to obtain $f(t)$ from equation 10, we apply Taylor expansion to the right hand of the equation and omit the high-order terms, which yields,

$$\int I_{sc}(t)dt = \frac{\mu_0}{R} \sum_{i=1}^{n} \iint (\nabla \varphi(\vec{r}) - \frac{\partial^2 \varphi}{\partial z \partial x} f(t)\vec{k} - \frac{\partial^2 \varphi}{\partial z \partial y} f(t)\vec{k} - \frac{\partial^2 \varphi}{\partial z \partial z} f(t)\vec{k}) \cdot d\overrightarrow{A_i} \tag{11}$$

Simplifying equation 11 yields,

$$\int I_{sc}(t)dt = \frac{\mu_0}{R} (\sum_{i=1}^{n} \iint \nabla \varphi(\vec{r}) \cdot d\overrightarrow{A_i} - f(t) \sum_{i=1}^{n} \iint (\frac{\partial^2 \varphi}{\partial z \partial x}\vec{k} + \frac{\partial^2 \varphi}{\partial z \partial y}\vec{k} + \frac{\partial^2 \varphi}{\partial z \partial z}\vec{k}) \cdot d\overrightarrow{A_i}) \tag{12}$$

As a result, the localized movement of the PFM $f(t)$ can be expressed as a function of the obtained short circuit current signal as below,

$$f(t) = \frac{\frac{\mu_0}{R} \sum_{i=1}^{n} \iint \nabla \varphi(\vec{r}) \cdot d\overrightarrow{A_i} - \int I_{sc}(t)dt}{\frac{\mu_0}{R} \sum_{i=1}^{n} \iint (\frac{\partial^2 \varphi}{\partial z \partial x}\vec{k} + \frac{\partial^2 \varphi}{\partial z \partial y}\vec{k} + \frac{\partial^2 \varphi}{\partial z \partial z}\vec{k}) \cdot d\overrightarrow{A_i}} \tag{13}$$

Thus, we have provided a theoretical model to obtain the localized movement of the internal tissue using our PFM-based bioelectronics. The obtained electrical signal from the PFM-based liquid bioelectronics can therefore be used to interpret the local biomechanics of the internal tissue.

Supplementary Note 10. Comparison between ferromagnetic liquid droplets and PFM

The PFM in this work differs from the previously reported ferromagnetic liquid droplets (FMLD)[1] in four aspects.

First, the materials usage and materials science in our PFM systems are different from those of the FMLD systems. (1) We use nanoscale permanent magnetic particles (NdFeB, ~ 100 nm) to construct our PFM, whereas FMLD adopts iron oxide (Fe_3O_4, ~20 nm). The NdFeB nanomagnets retain their permanent magnetism in the nanoscale. However, the iron oxide becomes superparamagnetic, rendering ferrofluid a paramagnetic material. (2) The iron oxide nanoparticles used in these reports were coated with a layer of surfactant (oleic acid, ~ 4 nm) whereas the NdFeB nanomagnets were coated with a silica nanolayer. (3) In terms of carrier fluids, we have demonstrated the universality of PFM in various carrier fluids including non-aqueous and aqueous solutions, as long as the viscosity requirement is met. In contrast, prior works on FMLD used water-based ferrofluids. A prerequisite for the formation of FMLD is the usage of amine-modified polyhedral oligomeric silsesquioxane ($POSS-NH_2$) in toluene solution, which can assemble and become anchored onto the iron oxide nanoparticles at the oil-water interface to induce the interface jamming.

Second, the formation mechanism of our PFM is distinct from that of FMLD. FMLD relies on the interfacial assembly and jamming of paramagnetic iron oxide at the interface between an aqueous phase containing functionalized nanoparticles (NPs) and a toluene solution with functionalized ligands. This interfacial jamming restricts the translation and rotational degree of the freedom of the NPs and enhances the magnetic dipole interactions between adjacent NPs by increasing the packing density. This jamming phenomenon can be considered as a liquid-to-glass transition, which generates a two-dimensional layer of NPs on the curved surface and produces a remanent magnetization of the droplet. On the contrary, we create the PFM through the construction of a three-dimensional ORM network structure inside the carrier fluid. We are decoupling the particle Brownian motion and colloidal stability in condensed matter to invent the PFM systems with high permanent magnetization, flowability, and reconfigurability. This is an innovation in the community of both materials science and condensed matter physics, since creating a permanent magnetism in a colloidal magnetic suspension via dipole-dipole interaction remains an open question. The key approach will be to construct a three-dimensional ramified nanomagnet network with oriented magnetic moments in a viscous fluid where Brownian motion will be minimized, and the network structure can defy particle gravity to ensure colloidal stability. The network structure spans the entire 3D volume of the PFM droplet, not just the surface, and generates a remnant magnetization along a certain direction while maintaining the gravitational stability of the droplet through the poroelasticity of the 3D network structure. The formation of the 3D ORM network can be considered as a directional strong flocculation based on magnetic dipole interaction. Instead of utilizing dense packing to restrict the random movement of the surface NPs as in FMLD, we employ strong interparticle magnetic interactions to restrict the movement of NdFeB nanomagnets in the PFM. To ensure the formation of a loose network structure rather than a dense aggregate (as seen in pure deionized water), an appropriate viscosity of the carrier fluid is

required to tune the kinetics, such as the diffusion length of the NdFeB during the self-assembly process. In this way, our PFM can be considered a special type of volumetric jamming, rather than the surface jamming observed in the FMLD.

Third, the properties of our PFM significantly differ from those of FMLD, due to the distinct formation mechanisms. (1) One notable difference lies in the formation timescale. Based on the prior studies, the formation of FMLD occurs within a time range of minutes, varying from a few to several hundred minutes, which is limited by the interfacial magnetic NP-surfactants assembly process. On the contrary, our PFM is formulated within seconds upon an external impulsed magnetic field. (2) Our PFM displays enhanced magnetic properties compared to FMLD. The remanence of our PFM reaches up to 46.03 emu g^{-1}, approximately four times of magnitude higher than that of the FMLD. Similarly, the coercivity of our PFM reaches 699.91 Oe, 7.7 times higher than the value obtained in FMLD. These results indicate that our PFM possesses stronger permanent magnetism than the FMLD, which we attribute to the higher utilization efficiency of the magnetic nanoparticles. (3) In our PFM, the entire ensemble of dispersed nanomagnets contributes to the magnetism, as opposed to FMLD, where only a densely packed surface layer participates. (4) Moreover, our PFM demonstrates better stability under an external magnetic field compared to the FMLD. Previous studies have shown that an external magnetic field of less than 20 mT can be utilized to manipulate the physical orientation of FMLD. However, exceeding this threshold may cause the magnetization of individual magnetic NP-surfactants to switch, potentially resulting in instability and disassembly of the FMLD. Our PFM is capable of being manipulated by higher external magnetic fields, up to 69 mT.

Fourth, the application scenarios of our PFMs significantly differ from those of FMLD systems. Our PFM was used as liquid biosensors that utilize reconfigurable magnetism to wirelessly quantify cardiovascular functions in a self-powered manner. However, FMLD systems were used as actuators remotely controlled by an external magnetic field for sorting and spatial arranging. In future potential applications, since PFM shows better stability and flexibility, it will be suitable for a wide range of scenarios. For instance, PFM holds great potential for deployment as a liquid-based robotic system in undersea environments. Its applications encompass undersea exploration, facilitating oxygen transportation. Additionally, PFM can serve as a high-precision magnetic sensor, enhancing diver navigation, communication, situational awareness, and threat detection capabilities. In contrast, FMLD has limitations in performing complex tasks as it relies solely on the interface between two distinct liquid media. Thus, the application of FMLD is limited to operating exclusively within liquid interfaces.

In summary, our PFM is fundamentally different from the reported FMLD in terms of materials, formation mechanism, associated magnetic properties, and application scenarios. Compared to the FMLD, our PFM offers several advantages including the absence of surfactants or the need for two immiscible fluids, faster formation speed, stronger permanent magnetism, and improved stability.

Supplementary Table 1. Comparison of the coercivity with different fluidic magnetic systems

System	Format	Carrier fluid	Coercivity	Ref.
Fe_3O_4-CO_2H	Particles	Amine-modified polyhedral oligomeric silsesquioxane	~90.48 Oe	1
$BaFe_{1.5}Sc_{0.5}O_{19}$	Platelets	Nematic liquid crystal	~70 Oe	11
NdFeB @SiO_2	Particles	Silicone fluid/alginate	~699.91 Oe	This work

Supplementary References

1. Liu, X.*, et al.* Reconfigurable ferromagnetic liquid droplets. *Science* **365**, 264-267 (2019).

2. Wang, Z., Holm, C. & Müller, H.W. Molecular dynamics study on the equilibrium magnetization properties and structure of ferrofluids. *Phys. Rev. E* **66**, 021405 (2002).

3. Rovigatti, L., Russo, J. & Sciortino, F. Structural properties of the dipolar hard-sphere fluid at low temperatures and densities. *Soft Matter* **8**, 6310-6319 (2012).

4. Kristóf, T. & Szalai, I. Magnetic properties and structure of polydisperse ferrofluid models. *Phys. Rev. E* **68**, 041109 (2003).

5. Chow, T.L. *Introduction to electromagnetic theory: a modern perspective*, (Jones & Bartlett Learning, 2006).

6. Kim, C.*, et al.* Gravitational stability of suspensions of attractive colloidal particles. *Phys. Rev. Lett.* **99**, 028303 (2007).

7. Buscall, R. & White, L.R. The consolidation of concentrated suspensions. Part 1.—The theory of sedimentation. *J. Chem. Soc., Faraday Trans. 1* **83**, 873-891 (1987).

8. Buscall, R. The sedimentation of concentrated colloidal suspensions. *Colloids Surf.* **43**, 33-53 (1990).

9. Zia, R.N., Landrum, B.J. & Russel, W.B. A micro-mechanical study of coarsening and rheology of colloidal gels: Cage building, cage hopping, and Smoluchowski's ratchet. *J. Rheol.* **58**, 1121-1157 (2014).

10. Manley, S., Skotheim, J.M., Mahadevan, L. & Weitz, D.A. Gavitational collapse of colloidal gels. *Phys. Rev. Lett.* **94**, 218302 (2005).

11. Mertelj, A., Lisjak, D., Drofenik, M. & Copic, M. Ferromagnetism in suspensions of magnetic platelets in liquid crystal. *Nature* **504**, 237-241 (2013).